Applied Catalysis B: Environment and Energy 357 (2024) 124310

Contents lists available at ScienceDirect

Applied Catalysis B: Environment and Energy

journal homepage: www.elsevier.com/locate/apcatb

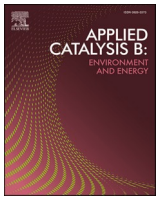

Incorporating a binuclear cobalt polymer into mesoporous TiO_2 to construct a new Z-scheme heterojunction for boosting artificial photosynthesis

Yun-Nan Gong, Shan Wang, Hui-Jun Dong, Jian-Hua Mei, Di-Chang Zhong *, Tong-Bu Lu *

Institute for New Energy Materials and Low Carbon Technologies, School of Materials Science and Engineering, School of Chemistry and Chemical Engineering, Tianjin University of Technology, Tianjin 300384, China

ARTICLE INFO

Keywords:
Z-scheme heterojunction
Mesoporous TiO_2
Binuclear cobalt complex
Artificial photosynthesis

ABSTRACT

The construction of photocatalysts with Z-scheme heterojunction structures has been regarded as an effective strategy to enhance catalytic efficiency in artificial photosynthesis. However, the reported Z-scheme heterojunctions usually show small interfacial contact area, which are unbeneficial for highly efficient charge separation. Herein, a host-guest strategy was developed to precisely construct Z-scheme heterojunctions, with which a polymer (Co_2-P) containing binuclear cobalt catalytic centers was incorporated into the pores of mesoporous TiO_2, affording a new Z-scheme heterojunction of Co_2-P@TiO_2 with surrounding contact interfacial between Co_2-P and TiO_2. As a result, the resulting Co_2-P@TiO_2 heterojunction possesses large interfacial contact areas, and thereby exhibits an outstanding photocatalytic activity for the reduction of CO_2 to CO with H_2O as the electron donor. The CO production rate reaches as high as 139.2 μmol g^{-1} h^{-1}, which is 4.0, 4.2 and 3.1 times higher than the pristine TiO_2, Co_2-P, and a Z-scheme heterojunction of Co_2-P/TiO_2 conventionally prepared, respectively. Systematic studies demonstrate that the encapsulation of Co_2-P into the pores of mesoporous TiO_2 greatly accelerates charge separation and electron transfer, thus accounting for its enhanced photocatalytic activity. This study paves a new way to design efficient catalysts for artificial photosynthesis.

1. Introduction

The excessive emission of carbon dioxide (CO_2) has resulted in serious environmental problem [1,2]. Inspired by the natural photosynthesis, researchers believe that the conversion of CO_2 and H_2O into carbohydrates and O_2 by solar energy could be a promising approach to alleviate the environmental issue caused by the greenhouse gas CO_2 [3–5]. Nevertheless, it is still daunting to combine CO_2 reduction and H_2O oxidation with high catalytic efficiency in one photocatalytic system due to the inherent chemical inertness of both CO_2 and H_2O molecules [6–11]. Recently, various strategies have been developed to construct photocatalysts to achieve artificial photosynthesis [12–16], among which the fabrication of heterojunctions from different semiconductors (SC) is regarded as an effective strategy, as the heterojunction photocatalysts usually exhibit enhanced separation of photogenerated electron-hole pairs over single component [17–21]. Among heterojunction photocatalysts, Z-scheme heterojunction photocatalysts possess a unique advantage over other heterojunctions because of their improved position of both conduction and valence bands, not only hindering the rapid electron-hole recombination, but also enhancing the oxidation and reduction abilities [22–25]. At present, three main strategies have been developed to construct Z-scheme heterojunctions. The first one is to load small semiconductor nanoparticles on the surface of bulky semiconductors. The second one is to integrate two semiconductor nanoparticles with protected organic ligands. The third one is to compose semiconductor nanoparticles with Janus configuration. However, these Z-scheme heterojunctions often show small interfacial contact area (Scheme 1a), which are unbeneficial for accelerating charge separation [19–25]. Therefore, it is highly desired to develop efficient Z-scheme heterojunction photocatalysts for greatly promoting charge separation toward artificial photosynthesis.

Porous materials featuring high porosity and surface area, has attracted tremendous attention in photocatalytic CO_2 reduction. They are not only favorable to the transport of substrates and products, but also have capability for the encapsulation of functional molecules inside the pores to form composites to greatly facilitate charge separation and

* Corresponding authors.
E-mail addresses: dczhong@email.tjut.edu.cn (D.-C. Zhong), lutongbu@tjut.edu.cn (T.-B. Lu).

https://doi.org/10.1016/j.apcatb.2024.124310
Received 7 April 2024; Received in revised form 3 June 2024; Accepted 14 June 2024
Available online 17 June 2024

further to enhance photocatalytic activity [26–30]. For example, Deng and coworkers prepared a series of metal-organic framework (MOF)--based composites by growing TiO_2 inside different pores of chromium-based MOFs for CO_2 photoreduction, which exhibit significantly enhanced catalytic activity for the reduction of CO_2 to CO and CH_4 compared with the pristine MOFs and TiO_2 [29]. Chen et al. developed a new catalytic system by encapsulating the cationic photosensitizer $[Ru(phen)_3]^{2+}$ (phen = 1,10-phenanthroline) into the pores of an anionic MOF via electrostatic interaction, which shows an outstanding photocatalytic activity for the reduction of CO_2 to CO with triethanolamine (TEOA) as the electron donor [30]. Although many efforts have been devoted in this field, to our knowledge, the encapsulation of functional units into the pores of porous materials to construct Z-scheme heterojunctions for CO_2 photoreduction has not been documented so far.

As an important porous semiconductor, mesoporous TiO_2 has been recognized its great potential in photocatalysis due to its non-toxicity, low cost and high stability [31–34]. Although the photogenerated electrons and holes are prone to fast recombine in single mesoporous TiO_2, leading to low photocatalytic efficiency, mesoporous TiO_2 might be an ideal model for incorporating functional units into its pores to construct Z-scheme heterojunctions to improve charge separation efficiency. Herein, for the first time, we incorporated a polymer (Co_2-P) containing binuclear cobalt catalytic centers into the pores of mesoporous TiO_2 through host-guest strategy, to fabricate a Z-scheme heterojunction photocatalyst of Co_2-P@TiO_2 with surrounding contact interfacial between Co_2-P and TiO_2 for artificial photosynthesis (Scheme 1b). Strikingly, the resulting Co_2-P@TiO_2 heterojunction exhibits an excellent photocatalytic activity for the reduction of CO_2 to CO with H_2O as the electron donor, in absence of any additional photosensitizer and sacrificial agent. The CO generation rate of Co_2-P@TiO_2 is 4.0, 4.2 and 3.1 times higher than the pristine TiO_2, Co_2-P and a Z-scheme heterojunction of Co_2-P/TiO_2 conventionally prepared, respectively. The significantly enhanced photocatalytic performance of Co_2-P@TiO_2 heterojunction can be attributed to the improved charge separation efficiency, as demonstrated by the results of a series of photoelectrochemical experiments.

2. Experimental section

2.1. Materials and equipments

All chemicals were commercially available and used without further purification. Powder X-ray diffraction (XRD) patterns were recorded on D8 ADVANCEX-Ray Diffractometers with Cu Kα radiation (λ = 1.54 Å). Nitrogen sorption measurements were conducted at 77 K using a multistation specific surface micropore and vapor adsorption analyzer (BELSORP-Mas, Microtrac BEL, Japan). Solid-state UV–vis absorption spectra were obtained on a UV–vis spectrophotometer (UV-3600, Shimadzu, Japan). Photoluminescence (PL) spectra were measured with an F-4600 fluorescence spectrometer. X-ray photoelectron spectroscopy (XPS) measurements were conducted by using an X-ray spectrometer (ESCALAB 250 Xi spectrometer, Thermo Scientific, USA) with Al Kα as the excitation source. Scanning electron microscopy (SEM) and energy dispersive spectroscopy (EDS) mapping were acquired on a FEI-Quanta FEG 250 scanning electron microanalyzer. High-resolution transmission electron microscopy (HR-TEM) was conducted on transmission electron microscope with a LaB6 Gun (Tecnai G2 Spirit TWIN and Talos F200 X, FEI, USA) at an acceleration voltage of 120 kV. Raman spectra were recorded on a high-resolution laser confocal fiber Raman spectrometer (HORIBA EVOLUTION, HORIBA Jobinyvon, France). Liquid chromatography mass spectrometry (LC-MS) was conducted using a Waters LC-MS system (UPLC I Class/Xevo G2-S QTOF, United States). The Co content was quantified by an inductively coupled plasma mass spectrometer (ICP-MS, iCAP RQ, Germany). The isotopes of ^{13}C for CO and ^{18}O for O_2 were analyzed using mass spectrometry (HPR-20 QIC). The photocurrent, Mott-Schottky plots, and electrochemical impedance spectroscopy (EIS) measurements were performed on a CHI 660E electrochemical workstation. Fourier transform infrared spectroscopy (FT-IR) and *in situ* FT-IR spectra were recorded on Nicolet iS50 IR spectrometers, and samples were tableted with KBr as support. Electron paramagnetic resonance (EPR) measurements were performed on an electron paramagnetic resonance spectrometer (Bruker, EMXplus-6/1, Germany). The catalytic product in gaseous phase of the reaction system was analyzed by gas chromatography (GC-2014+ATF, 230 C, Shimadzu, Japan) equipped with two automated gas sampling valves, which contain a thermal conductivity detector (TCD) and a flame ionization detector (FID).

2.2. Synthesis of mesoporous TiO_2

Mesoporous TiO_2 was synthesized according to the literature [35]. Typically, 1.6 g Pluronic F127, 2.0 mL AcOH, and 3.0 mL concentrated HCl were added to 30 mL tetrahydrofuran (THF), which was stirred for 10 min. Afterwards, 3.0 mL tetrabutyl titanate and 0.20 mL H_2O were added dropwise into the above solution, which was stirred vigorously. The obtained golden-yellow solution was transferred to oven to evaporate THF at 45 °C for 24 h to form monomicelle gel, which was added

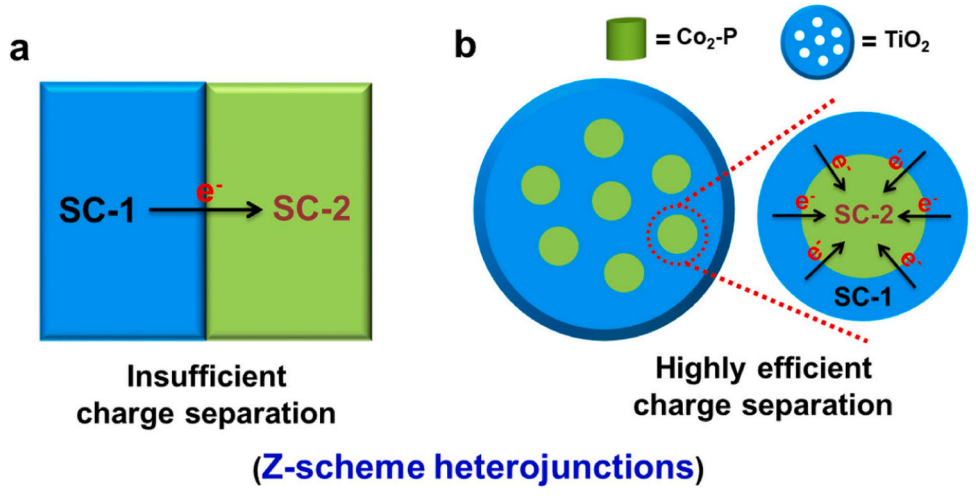

Scheme 1. Schematic representation of (a) the reported Z-scheme heterojunctions with insufficient charge separation and (b) the new Z-scheme heterojunction with highly efficient charge separation.

into a 50-mL Teflon-lined autoclave and heated at 70 °C for 24 h. After cooling down to room temperature, the precipitates were collected by centrifugation and dried. Finally, the mesoporous TiO_2 microspheres were obtained after pyrolyzing in a tubular furnace under N_2 at 350 °C for 3 h, following by calcining in air at 400 °C for 3 h.

2.3. Synthesis of binuclear cobalt complex (Co_2-Br)

First, the 2,6-diformyl-4-bromophenol was synthesized according to the literature [36]. Then, a mixture of $Co(ClO_4)_2{\cdot}6\ H_2O$ (548.9 mg, 1.5 mmol), 2,6-diformyl-4-bromophenol (0.344 g, 1.5 mmol), 2, 2-dimethyl-1,3-diaminopropane (177.8 μL, 1.5 mmol), triethylamine (1.0 mL) and ethanol (15.0 mL) was stirred for 20 h at room temperature. The precipitate of Co_2-Br was obtained by centrifugation and washed with ethanol and deionized water.

2.4. Synthesis of binuclear cobalt polymer (Co_2-P)

The Co_2-P was synthesized through Sonogashira–Hagihara coupling reaction. Typically, Co_2-Br (70.6 mg, 0.1 mmol) and 2,2-dimethyl-1,3-diaminopropane (20.2 mg, 0.1 mmol) were added in a mixed solvent of dimethylformamide (DMF) (10 mL) and triethylamine (13.2 mL), which was purged with N_2 for 20 min to remove the dissolved oxygen. Afterwards, the tetrakis(triphenylphosphine)palladium (34.6 mg, 0.03 mmol) was added into the above mixture, which was further purged with N_2 for 20 min. The mixture was stirred at 120 °C for 24 h. After cooling down to room temperature, the precipitate of Co_2-P was obtained by centrifugation and washed with DMF and methanol.

2.5. Synthesis of Co_2-P@TiO_2

First, Co_2-Br (70.6 mg, 0.1 mmol), 2,2-dimethyl-1,3-diaminopropane (20.2 mg, 0.1 mmol) and the tetrakis(triphenylphosphine)palladium (34.6 mg, 0.03 mmol) were added in a mixed solvent of DMF (10 mL) and triethylamine (13.2 mL), which was purged with N_2 for 20 min to remove the dissolved oxygen. Afterwards, the above mixture was injected into three-necked flask containing mesoporous TiO_2 (30.3 mg) under reduced pressure, which was stirred at 120 °C for 24 h. After cooling down to room temperature, the precipitate of Co_2-P@TiO_2 was obtained by centrifugation and washed with DMF and methanol.

2.6. EPR measurement

EPR measurements were carried out by using 5,5-dimethyl-1-pyrroline-N-oxide (DMPO) as the radical trapping agent, ·OH and $\cdot O_2^-$ can be trapped by DMPO to form DMPO-·OH and DMPO-$\cdot O_2^-$, respectively. 5.0 mg photocatalysts, 20 μL DMPO and 1.0 mL H_2O were added to 10 mL glass bottle for ·OH detection. In addition, 1.0 mL methanol was used to replace 1.0 mL H_2O to detect $\cdot O_2^-$ radicals. EPR measurements were performed in the dark and after 3 min of light irradiation.

2.7. Photocatalytic experiment

The photocatalytic CO_2 reduction measurements were carried out in a 50 mL sealed quartz bottle. First, 1.0 mg photocatalysts was dispersed into 400 μL ethyl acetate, which was deposited onto the surface of filter paper. Then, the filter paper and 20 μL deionized water was loaded into the reactor, which was degassed with CO_2 to remove O_2 and other gases, followed by a 300 W Xe lamp irradiation ($\lambda > 320$ nm). The generated gaseous products were analyzed with gas chromatography.

2.8. Photoelectrochemical measurement

Photocurrent and EIS measurements of Co_2-P@TiO_2, TiO_2, Co_2-P and Co_2-P/TiO_2 were performed via a standard three-electrode system in 0.1 M Na_2SO_4 solution with a working electrode, a platinum plate as the counter electrode, and a saturated Ag/AgCl electrode as a reference electrode. A 300 W xenon lamp was used as the light source. 2 mg sample was dispersed into a solution of 50 μL 5 wt% Nafion and 0.95 mL ethanol. Then, the mixture was deposited onto FTO surface with an area of 4 cm^2 and left in the air for drying to obtain working electrode. Photocurrent were recorded at 0.6 V. EIS measurement was carried out at −0.6 V in the dark.

2.9. In situ FT-IR spectra measurement

The *in situ* FT-IR spectra were collected under light irradiation with the incremental time upon the introduction of a mixture of CO_2/H_2O vapour. A mixture of 1.0 mg Co_2-P@TiO_2 and 50 mg KBr was ground for 10 min. Then the mixture was sealed in the chamber for purging with N_2 for 20 min.

2.10. In situ XPS measurement

In situ XPS were conducted on an X-ray spectrometer with Al Kα as the excitation source and a quzrtz light window. In a typical process, 2.0 mg Co_2-P@TiO_2 was ground for 10 min, which was sealed in the chamber and kept under vacuum. The XPS spectrum of Co_2-P@TiO_2 was first recorded in the dark. After visible light irradiation for 5 min, the XPS spectrum was recorded again.

3. Results and discussion

The powder XRD pattern of TiO_2 shows diffraction peaks at 27.4, 36.1, 39.1, 41.3, 43.9, 54.3, 56.6, 62.9, 64.0, 69.0, and 69.7, which can be assigned to the 110, 101, 200, 111, 210, 211, 220, 002, 310, 301, and 112 diffractions of rutile, indicating its highly crystalline phase (Fig. S1) [35]. The SEM image demonstrates that TiO_2 comprises the dehiscent microspheres with the size of about 4 μm (Fig. S2). N_2 adsorption measurement of TiO_2 at 77 K and 1 atm reveals a reversible type IV isotherm with an obvious hysteresis loop in the desorption isotherm, suggesting the presence of mesopores (Fig. S3). The Brunauer-Emmett-Teller (BET) surface area is 77.3 $m^2\ g^{-1}$ and the pore size distribution is 12–33 nm (Fig. S4). In addition, the LC-MS of Co_2-Br shows the ion peaks at *m/z* 750.93 and 860.06, corresponding to the species of $[(Co_2\text{-Br})(HCOO)]^+$ and $[(Co_2\text{-Br})(OH)(C_2H_5OH)\ (CH_3OH)\ (CH_3CN)]^+$, respectively (Fig. S5). Powder XRD pattern of Co_2-Br shows the amorphous natures (Fig. S6). The above results illustrate the successful synthesis of the mesoporous TiO_2 and the binuclear cobalt complex of Co_2-Br.

Subsequently, Co_2-Br, 4,4'-diethynylbiphenyl and tetrakis (triphenylphos-phine) palladium as a catalyst were introduced into the pores of mesoporous TiO_2, which was heated at 120 °C for 24 h to generate Co_2-P@TiO_2 composite with binuclear cobalt polymer (Co_2-P) incorporated into the pores of mesoporous TiO_2 (Scheme S1) [37,38]. The FT-IR spectrum of Co_2-P@TiO_2 exhibits a characteristic peak at 2207 cm^{-1}, which can be assigned to the stretching vibration of unsymmetrical alkyne bond (-C≡C-), suggesting the formation of alkynyl linkages (Fig. S7) [39,40]. The Raman spectrum of Co_2-P@TiO_2 shows a characteristic peak at 2208 cm^{-1}, corresponding to the unsymmetrical alkyne bonds (-C≡C-), further verifying the presence of alkynyl linkages (Fig. S8) [10]. The XPS of Co_2-P@TiO_2 shows the binding energies of C, N, O, Co and Ti (Fig. S9). Moreover, no palladium signal was observed in XPS spectrum, which may be attributed to its low concentration (0.83 wt%) in the Co_2-P@TiO_2 as realized from ICP-MS analysis. The powder XRD pattern of Co_2-P@TiO_2 is identical to that of TiO_2, implying the structural integrity of TiO_2 in Co_2-P@TiO_2 composite and the absence of long-range order of Co_2-P polymer (Fig. S10). The above results suggest that the Co_2-P with alkynyl linkages has been successfully synthesized on Co_2-P@TiO_2 composite. Additionally, the SEM image demonstrates that the size and morphology of Co_2-P@TiO_2 are almost identical to the pristine TiO_2 (Fig. 1a and S2). EDS mapping of

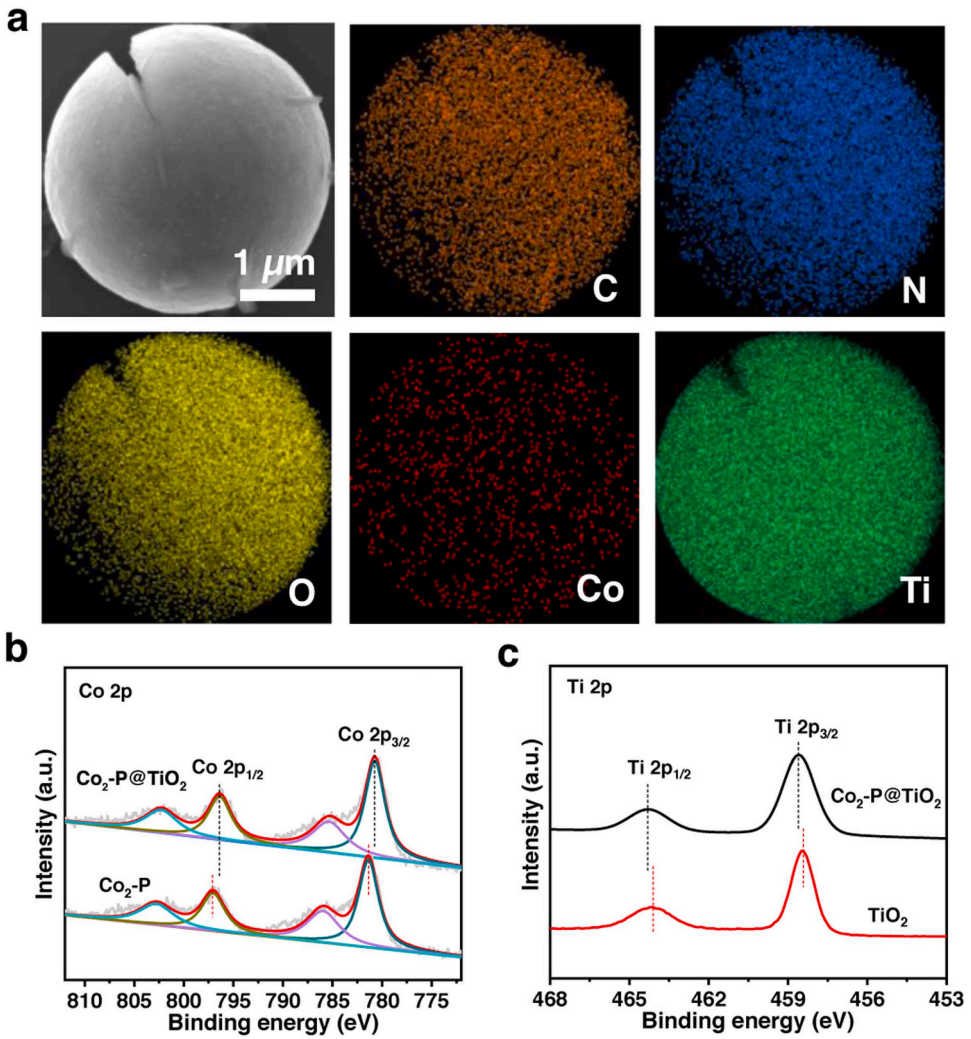

Fig. 1. (a) SEM image and EDS mapping of C, N, O, Co and Ti elements of Co_2-P@TiO_2. (b) XPS spectra for the Co 2p of Co_2-P and Co_2-P@TiO_2. (c) XPS spectra for the Ti 2p of TiO_2 and Co_2-P@TiO_2.

Co_2-P@TiO_2 reveals the homogeneous distribution of C, N, O, Co and Ti (Fig. 1a). TEM image of Co_2-P@TiO_2 demonstrates that some dark dots were observed, suggesting the incorporation of Co_2-P in TiO_2 (Fig. S11a). HR-TEM image of Co_2-P@TiO_2 shows clear interface between Co_2-P and TiO_2, and the lattice fringe of 0.32 nm is attributed to the (110) face of TiO_2 (Fig. S11b) [35]. The BET surface area and pore size of Co_2-P@TiO_2 are 16.2 m^2 g^{-1} and ~4.1 nm respectively, sharply reduced compared with the pristine TiO_2 (Figs. S3 and S4). These results suggest that the Co_2-P was successfully incorporated into the pores of mesoporous TiO_2 [41,42]. The ICP-MS analysis reveals that the Co content in Co_2-P@TiO_2 is 1.97 wt%, corresponding to the Co_2-P content of ~12.49 wt% in Co_2-P@TiO_2. In addition, for comparison, pure Co_2-P was also synthesized by the solvothermal reaction of Co_2-Br and 4, 4'-diethynylbiphenyl at 120 °C for 24 h. The FT-IR and Raman spectra of Co_2-P display obvious characteristic peaks at 2209 and 2208 cm^{-1} respectively, hinting the formation of alkynyl linkages (Figs. S12 and S13). The SEM image of Co_2-P shows cubic morphology with the size of approximately 300 nm (Fig. S14). The result of powder XRD pattern for Co_2-P demonstrates that it exhibits the amorphous natures (Fig. S6).

To reveal the valence and interfacial charge transfer of Co_2-P and Co_2-P@TiO_2, the XPS characterization was carried out. As shown in Fig. 1b, the XPS spectrum of Co_2-P shows two characteristic peaks at 781.3 and 797.0 eV in Co 2p spectrum, which can be attributed to the binding energies of Co $2p_{3/2}$ and Co $2p_{1/2}$, respectively. Furthermore, two corresponding satellite peaks at 785.9 and 802.8 eV are also observed, indicating that the oxidation state of Co species in Co_2-P is +2 [43,44]. For Co_2-P@TiO_2, the binding energies of Co $2p_{3/2}$ and Co $2p_{1/2}$ locate 780.7 and 796.4 eV, respectively. There are also two corresponding satellite peaks, demonstrating the +2 oxidation state of Co species in Co_2-P@TiO_2 (Fig. 1b). It is worth noting that the binding energies of Co $2p_{3/2}$ and Co $2p_{1/2}$ in Co_2-P@TiO_2 show negative shift compared with those in Co_2-P, and the binding energies of Ti $2p_{3/2}$ and Ti $2p_{1/2}$ in Co_2-P@TiO_2 displays positive shift compared with those in TiO_2 (Fig. 1c). These results imply that the electron transfers from TiO_2 to Co_2-P, and there are strong interfacial interactions between TiO_2 and Co_2-P.

The light absorbance of TiO_2 and Co_2-P was investigated by solid UV–vis spectra. As shown in Fig. 2a, the TiO_2 mainly absorb ultraviolet light. The band-gap energy (E_g) of TiO_2 is 3.00 eV, as estimated by the Kubelka-Munk (KM) method based on its solid UV–vis absorption spectroscopy (Fig. S15) [45–48]. By contrast, Co_2-P can abosrb both ultraviolet and visible lights with the E_g of 2.10 eV (Fig. 2a and S16). Moreover, Mott-Schottky measurements of TiO_2 and Co_2-P were performed with the frequencies of0.5, 1.0, and 1.5 kHz. The C^{2-} values (*vs.* applied potentials) of them show positive slopes, indicating that they exhibit the character of n-type semiconductors (Figs. 2b and 2c). The flat band potentials of them are about −1.18 and −1.34 V *vs.* Ag/AgCl (that is, −0.98 and −1.14 V *vs.* NHE) respectively, which are determined by the intersection points.

These values are equal to the lowest unoccupied molecular orbital

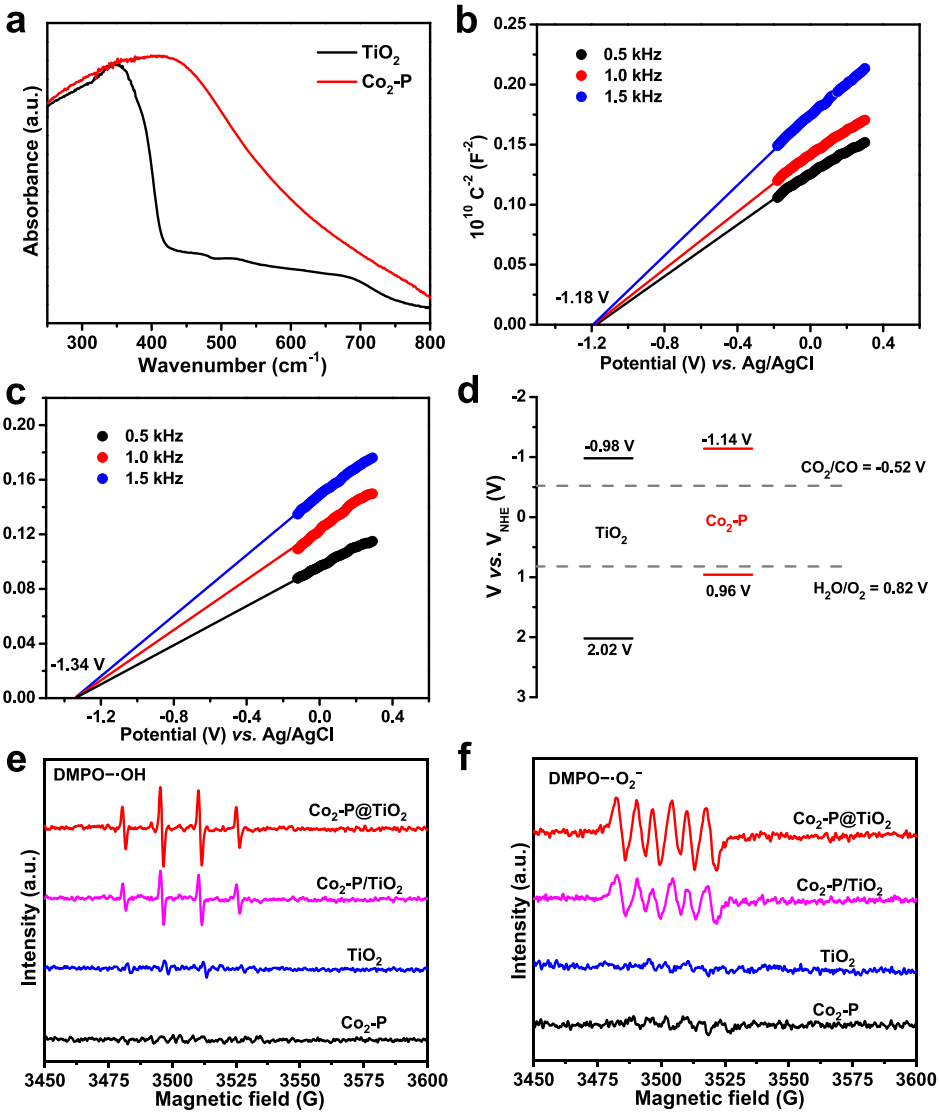

Fig. 2. (a) UV–vis spectra of TiO_2 and Co_2-P. (b) Mott−Schottky plots of TiO_2. (c) Mott−Schottky plots of Co_2-P. (d) Band-structure diagram for TiO_2 and Co_2-P. EPR spectra of (e) DMPO−·OH and (f) DMPO−·O_2^- for Co_2-P, TiO_2, Co_2-P@TiO_2 and Co_2-P/TiO_2 under light irradiation.

(LUMO). Therefore, the highest occupied molecular orbital (HOMO) of them are calculated to be 2.02 and 0.96 V *vs.* NHE, respectively (Fig. 2d). Obviously, the LUMO potentials of both TiO_2 and Co_2-P are more negative than those of photocatalytic CO_2 reduction reactions to CO (-0.52 V *vs.* NHE), CH_4 (-0.24 V *vs.* NHE), and HCOOH (-0.61 V *vs.* NHE), implying that they are theoretically feasible for photocatalytic CO_2 reduction. Moreover, the HOMO potentials of them are more positive than that of H_2O oxidation to O_2 (0.82 V) [11]. Additionally, TiO_2 and Co_2-P display a staggered band structure (Fig. 2d), suggesting that Z-scheme heterojunction in Co_2-P@TiO_2 composite may be formed upon light irradiation, which possibly improves the charge separation efficiency in photocatalytic CO_2 reduction [24].

To confirm if the Co_2-P@TiO_2 composite is the Z-scheme heterojunction photocatalyst, the EPR measurements of Co_2-P, TiO_2 and Co_2-P@TiO_2 with DMPO as a probe were carried out to monitor the generation of ·OH and ·O_2^- radicals [22–25]. As shown in Fig. 2e, the characteristic DMPO−·OH signals of TiO_2 and Co_2-P@TiO_2 were observed under light irradiation, while no distinct DMPO−·OH signal was observed for Co_2-P, owing to its insufficient oxidizing potential (0.96 V *vs.* NHE) for the oxidation of H_2O to ·OH (1.90 V *vs.* NHE) [49]. We note that Co_2-P@TiO_2 shows stronger DMPO−·OH signals than TiO_2, suggesting that more photogenerated holes of TiO_2 on Co_2-P@TiO_2 composite are retained compared with the pristine TiO_2. In addition, the characteristic signals of DMPO−·O_2^- were detected for Co_2-P, TiO_2 and Co_2-P@TiO_2, among which Co_2-P@TiO_2 exhibits stronger DMPO−·O_2^- signals than both Co_2-P and TiO_2, implying more photogenerated electrons of Co_2-P on Co_2-P@TiO_2 composite than the pristine Co_2-P and TiO_2 (Fig. 2f). Moreover, no DMPO−·OH and DMPO−·O_2^- signals were detected in the dark for Co_2-P, TiO_2 and Co_2-P@TiO_2, demonstrating that the ·OH and ·O_2^- species were produced by photogenerated holes and electrons, respectively (Figs. S17 and S18). The above results strongly confirm that the Z-scheme heterojunction was formed between Co_2-P and TiO_2 in Co_2-P@TiO_2 composite *via* electrostatic interactions upon light irradiation, which can promote charge separation in photocatalysis (Fig. S19

and Scheme S2). Also, the alkyne bonds (-C≡C-) in Co_2-P can be used as the electron withdrawing group to further facilitate charge transfer between TiO_2 and Co_2-P in Co_2-P@TiO_2 [50]. For comparison, a Z-scheme heterojunction of Co_2-P/TiO_2 was also conventionally fabricated by simply physical mixture of Co_2-P and TiO_2 *via* electrostatic interactions (Figs. 2e, 2f and S19).

Encouraged by the analysis above, the photocatalytic CO_2 reduction reactions over Co_2-P@TiO_2, TiO_2, Co_2-P and Co_2-P/TiO_2 were conducted in a CO_2-saturated gas-solid reactor with H_2O as the electron

donor. For all evaluated photocatalysts, the CO is the main reduction product with a small quantity of H_2 by-product. After 8 h of light irradiation, the CO yield of Co_2-P@TiO_2 is 1113.6 μmol g^{-1} (corresponding to the production rate of 139.2 μmol g^{-1} h^{-1}). In sharp contrast, TiO_2, Co_2-P and Co_2-P/TiO_2 exhibit significantly lower CO generation rates of 34.9, 32.9 and 44.8 μmol g^{-1} h^{-1}, respectively (Fig. 3a and S20). The photocatalytic activity of Co_2-P@TiO_2 is about 4.0, 4.2 and 3.1 times higher than those of TiO_2, Co_2-P and Co_2-P/TiO_2, manifesting the best photocatalytic activity of Co_2-P@TiO_2 for CO_2 reduction among the tested photocatalysts. Furthermore, the CO generation rate of Co_2-P@TiO_2 is superior to most of the reported heterogeneous photocatalysts by using H_2O as the electron donor (Table S1). The excellent activity of Co_2-P@TiO_2 could be attributed to the construction of Z-scheme heterojunction between Co_2-P and TiO_2. It should be noted that though Co_2-P/TiO_2 is also a Z-scheme heterojunction constructed from two same semiconductors of Co_2-P and TiO_2, the photocatalytic activity of Co_2-P/TiO_2 is only slightly higher than those of Co_2-P and TiO_2. These results illustrate that the greatly enhanced photocatalytic activity of Co_2-P@TiO_2 is not only related with formation of Z-scheme heterojunction, but also closely related with the formation mode of the Z-scheme heterojunction. In Co_2-P@TiO_2, Co_2-P is incorporated into the pores of mesoporous TiO_2, thus the interfacial contact area between Co_2-P and TiO_2 is much larger than that in Co_2-P/TiO_2. In this case, the photogenerated electrons of TiO_2 could quickly transfer to Co_2-P from all around, thus the reaction dynamics of CO_2 reduction over Co_2-P@TiO_2 could be greatly accelerated in contrast to Co_2-P/TiO_2 with smaller interfacial contact area and only one direction of electron injection (Scheme 1). This result demonstrates that the incorporation of Co_2-P into the pores of mesoporous TiO_2 to form Z-scheme heterojunction is an effective strategy to improve catalytic performance for CO_2 photoreduction. In addition to CO, low H_2 production rates of 11.8, 6.6, 10.2 and 3.0 μmol g^{-1} h^{-1} are detected for Co_2-P@TiO_2, TiO_2, Co_2-P and Co_2-P/TiO_2, respectively (Fig. S21), revealing that most photogenerated electrons take part in the CO_2 reduction with CO selectivities of 92.2, 84.1, 76.3 and 93.7 %, respectively. Additionally, the O_2 was also detected in the catalytic system, with the O_2 formation rate of 75.4 μmol g^{-1} h^{-1} for Co_2-P@TiO_2. Note that the stoichiometric ratio of CO/H_2 and O_2 is about 2:1, suggesting the mode of artificial photosynthesis (Fig. 3b). Additionally, the apparent quantum efficiency of Co_2-P@TiO_2 was 0.022 %, which was measured at 365 nm.

A series of control experiments demonstrate that negligible and even no CO product was detected in the absence of Co_2-P@TiO_2, CO_2, H_2O or light irradiation (Fig. S22). To confirm the carbon source of CO generated, the $^{13}CO_2$ isotope trace experiment for Co_2-P@TiO_2 was carried out. The mass spectrum (MS) shows a ^{13}CO signal peak at m/z = 29, verifying that the carbon source of CO originates from CO_2 (Fig. 3c) [6]. Moreover, the $H_2^{18}O$ isotope trace experiment over Co_2-P@TiO_2 was conducted to identify the electron source for photocatalytic CO_2 reduction to CO. The result of MS exhibits a signal peak at m/z = 36, which is attributed to $^{18}O_2$, confirming that the electron source for CO_2 photoreduction comes from the oxidation of H_2O (Fig. S23) [6]. The catalytic durability of Co_2-P@TiO_2 was further evaluated. As shown in Fig. 3d, the photocatalytic activity for CO_2 reduction of Co_2-P@TiO_2 is retained during the five consecutive cycles. The powder XRD and Raman spectrum of Co_2-P@TiO_2 after the photocatalytic reaction are similar to those of freshly prepared (Figs. S24 and S25). These results demonstrate the excellent stability of Co_2-P@TiO_2 during the photocatalytic CO_2 reduction reaction.

To illustrate the higher photocatalytic activity of Co_2-P@TiO_2 over TiO_2, Co_2-P and Co_2-P/TiO_2, photocurrent, EIS and PL measurements of them were performed [51,52]. As shown in Fig. 4a, Co_2-P@TiO_2 shows the highest photocurrent response among the four tested photocatalysts, demonstrating that it has the most efficient charge separation. The results of EIS indicate that in comparison with TiO_2, Co_2-P and TiO_2/-Co_2-P, Co_2-P@TiO_2 exhibits the smallest semicircle radius, implying its lowest charge-transfer resistance (Fig. S26). The PL spectra show that

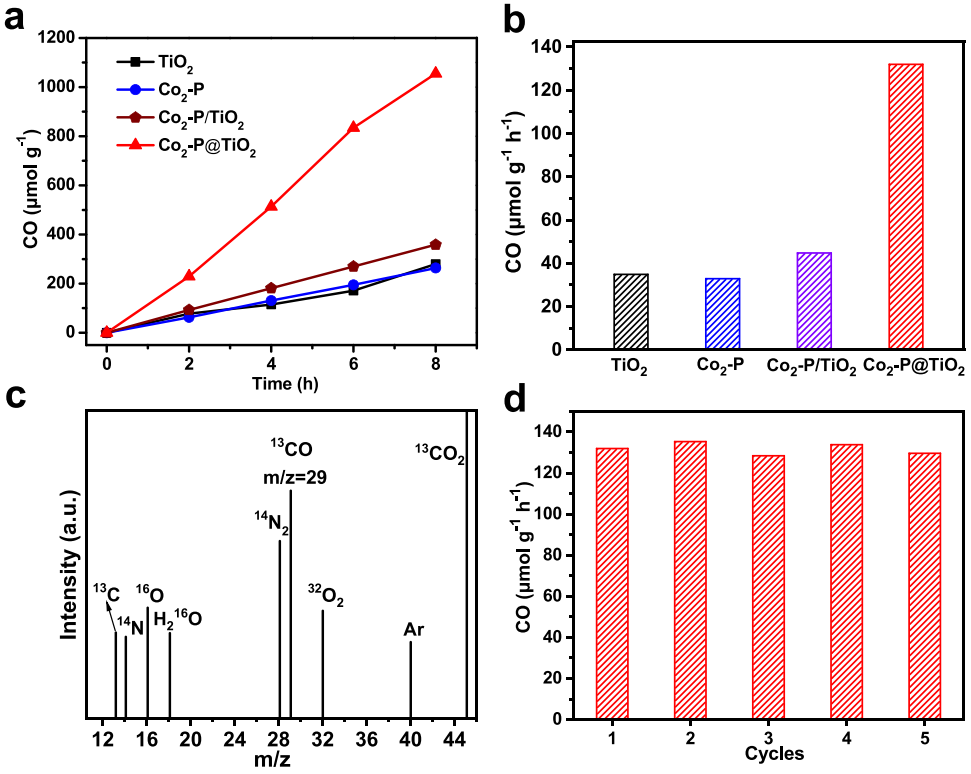

Fig. 3. (a) Time-dependent CO generation in photocatalytic CO_2 reduction over Co_2-P@TiO_2, TiO_2, Co_2-P and Co_2-P/TiO_2. (b) Yields of reduced and oxidized products over Co_2-P@TiO_2. (c) Mass spectrum of the gaseous product generated in the photocatalytic $^{13}CO_2$ reduction over Co_2-P@TiO_2. (d) The production rate of CO in five consecutive catalytic cycles over Co_2-P@TiO_2.

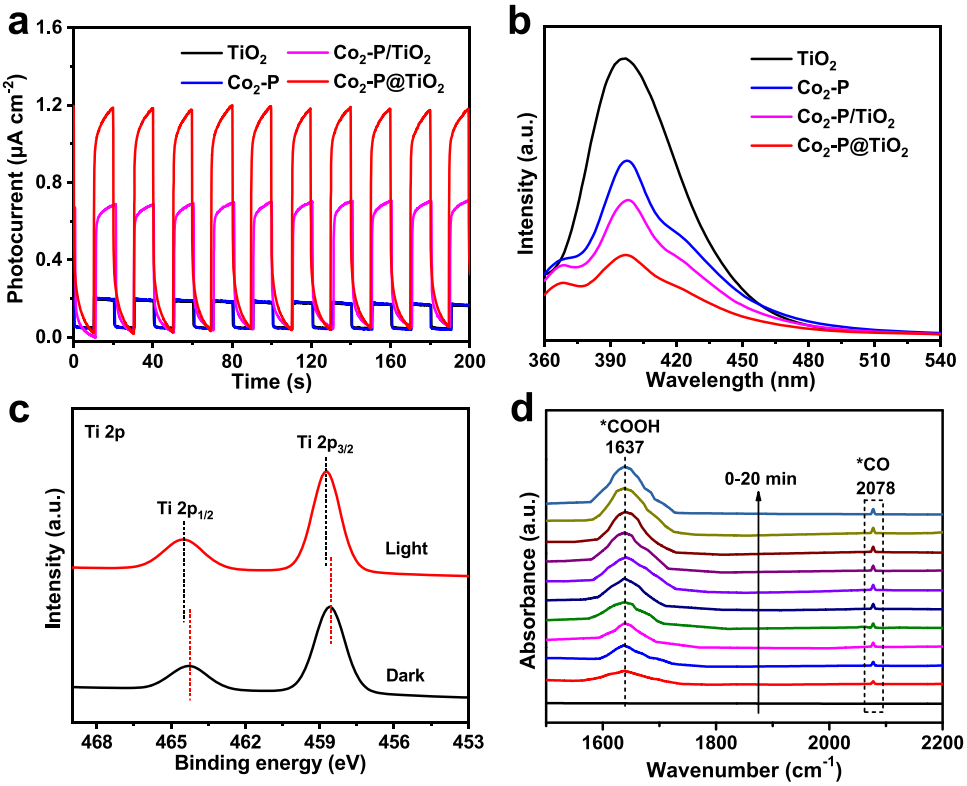

Fig. 4. (a) Photocurrent tests and (b) PL spectra of Co_2-P@TiO_2, TiO_2, Co_2-P and TiO_2/Co_2-P. (c) XPS spectra for Ti 2p of Co_2-P@TiO_2 in the dark and upon light irradiation. (d) *In situ* FTIR spectra of Co_2-P@TiO_2 in the process of photocatalytic CO_2 reduction.

the emission intensity of Co_2-P@TiO_2 is the weakest among all tested photocatalysts, suggesting that it has the fastest electron transfer (Fig. 4b). All the above results well support the best photocatalytic activity of Co_2-P@TiO_2 for CO_2 reduction among the tested catalysts. These results also demonstrate that the incorporation of Co_2-P into the pores of mesoporous TiO_2 could really form a new Z-scheme heterojunction which can greatly accelerates the charge separation and electron transfer, thereby boosting the catalytic reaction dynamics of artificial photosynthesis.

The possible catalytic mechanism for CO_2 photoreduction coupled with H_2O oxidation over Co_2-P@TiO_2 were revealed by *in situ* XPS measurements. The Ti $2p_{3/2}$ and Ti $2p_{1/2}$ binding energies of Co_2-P@TiO_2 locate at 458.5 and 464.2 eV in the dark, which shows positive shift to 458.8 and 464.5 eV respectively upon light irradiation (Fig. 4c). Moreover, the O 1 s binding energy of Ti-O bond also displays positive shift after light irradiation. These results imply that TiO_2 donates electron (Fig. S27). By contrast, the Co $2p_{3/2}$ and Co $2p_{1/2}$ binding energies of Co_2-P@TiO_2 exhibits negative shift upon light irradiation compared with those in the dark, suggesting that the Co^{2+} accepts electron (Fig. S28). As Co_2-P@TiO_2 is a Z-scheme heterojunction, upon light irradiation, both Co_2-P and TiO_2 of Co_2-P@TiO_2 harvest light to generate electron-hole pairs, where the photogenerated electrons in the LUMO of TiO_2 are transferred to the HOMO of Co_2-P to combine with photogenerated holes. The retained photogenerated holes in the HOMO of TiO_2 can oxidize H_2O to O_2, and the photogenerated electrons in the LUMO of Co_2-P are able to reduce adsorbed CO_2 to CO (Scheme S2). In order to monitor the key intermediates during the process of CO_2 photoreduction to CO over Co_2-P@TiO_2, *in situ* FTIR measurements were performed. As shown in Fig. 4d, new infrared peaks at 1637 and 2028 cm^{-1} were detected, and their intensities gradually increase along with the incremental irradiation time. The two new peaks can be assigned to the signals of *COOH and *CO intermediates respectively, which are regarded as the key intermediates for CO generation in CO_2 reduction reaction [53,54].

4. Conclusions

In summary, by incorporation of binuclear cobalt polymer into the pores of mesoporous TiO_2, a new Z-scheme heterojunction of Co_2-P@TiO_2 with surrounding interfacial contact area between Co_2-P and TiO_2 was successfully constructed, which exhibits an excellent catalytic activity for CO_2 photoreduction to CO with H_2O as the electron donor, without addition of any photosensitizer and sacrificial agent. The CO production rate reaches as high as 139.2 μmol g^{-1} h^{-1}, which is 4.0, 4.2 and 3.1 times higher than TiO_2, Co_2-P and the conventionally prepared Z-scheme heterojunction of Co_2-P/TiO_2, respectively. Photoelectrochemical experiments unveil that in comparison with TiO_2, Co_2-P and Co_2-P/TiO_2, Co_2-P@TiO_2 exhibits the highest charge separation efficiency, which clearly accounts for its best catalytic activity. The results of *in situ* FTIR demonstrate that both *COOH and *CO reaction intermediates were successfully detected for the formation of CO. This work provides a facile approach to develop efficient catalysts for artificial photosynthesis.

CRediT authorship contribution statement

Shan Wang: Investigation. **Yun-Nan Gong:** Writing – review & editing, Writing – original draft, Investigation. **Jian-Hua Mei:** Investigation. **Hui-Jun Dong:** Investigation. **Tong-Bu Lu:** Supervision. **Di-Chang Zhong:** Supervision, Conceptualization.

Declaration of Competing Interest

The authors declare that they have no known competing financial interests or personal relationships that could have appeared to influence the work reported in this paper.

Data Availability

Data will be made available on request.

Acknowledgements

This work was supported by National Key R&D Program of China (2022YFA1502902), the National Natural Science Foundation of China (22371208, 22271218, 22071182, 21931007).

Appendix A. Supporting information

Supplementary data associated with this article can be found in the online version at doi:10.1016/j.apcatb.2024.124310.

References

[1] S.J. Davis, K. Caldeira, H.D. Matthews, Future CO_2 emissions and climate change from existing energy infrastructure, Science 329 (2010) 1330–1333.
[2] C.L. Quéré, G.P. Peters, P. Friedlingstein, R.M. Andrew, J.G. Canadell, S.J. Davis, R. B. Jackson, M.W. Jones, Fossil CO_2 emissions in the post-COVID-19 era, Nat. Clim. Change 11 (2021) 197–199.
[3] B. Zhang, L. Sun, Artificial photosynthesis: opportunities and challenges of molecular catalysts, Chem. Soc. Rev. 48 (2019) 2216–2264.
[4] E.A.R. Cruz, D. Nishiori, B.L. Wadsworth, N.P. Nguyen, L.K. Hensleigh, D. Khusnutdinova, A.M. Beiler, G.F. Moore, Molecular-modified photocathodes for applications in artificial photosynthesis and solar-to-fuel technologies, Chem. Rev. 122 (2022) 16051–16109.
[5] S. Yoshino, T. Takayama, Y. Yamaguchi, A. Iwase, A. Kudo, CO_2 reduction using water as an electron donor over heterogeneous photocatalysts aiming at artificial photosynthesis, Acc. Chem. Res. 55 (2022) 966–977.
[6] L.-Y. Wu, Y.-F. Mu, X.-X. Guo, W. Zhang, Z.-M. Zhang, M. Zhang, T.-B. Lu, Encapsulating perovskite quantum dots in iron-based metal-organic frameworks (MOFs) for efficient photocatalytic CO_2 reduction, Angew. Chem. Int. Ed. 58 (2019) 9491–9495.
[7] L. Zhang, R.-H. Li, X.-X. Li, J. Liu, W. Guan, L.-Z. Dong, S.-L. Li, Y.-Q. Lan, Molecular oxidation-reduction junctions for artificial photosynthetic overall reaction, PNAS 119 (2022) e2210550119.
[8] W. Lin, J. Lin, X. Zhang, L. Zhang, R.A. Borse, Y. Wang, Decoupled artificial photosynthesis via a catalysis-redox coupled COF||$BiVO_4$ photoelectrochemical device, J. Am. Chem. Soc. 145 (2023) 18141–18147.
[9] N.-Y. Huang, J.-Q. Shen, X.-W. Zhang, P.-Q. Liao, J.-P. Zhang, X.-M. Chen, Coupling ruthenium bipyridyl and cobalt imidazolate units in a metal-organic framework for an efficient photosynthetic overall reaction in diluted CO_2, J. Am. Chem. Soc. 144 (2022) 8676–8682.
[10] Y. Wang, X. Shang, J. Shen, Z. Zhang, D. Wang, J. Lin, J.C.S. Wu, X. Fu, X. Wang, C. Li, Direct and indirect Z-scheme heterostructure-coupled photosystem enabling cooperation of CO_2 reduction and H_2O oxidation, Nat. Commun. 11 (2020) 3043.
[11] Y.-N. Gong, X. Guan, H.-L. Jiang, Covalent organic frameworks for photocatalysis: synthesis, structuralfeatures, fundamentals and performance, Coord. Chem. Rev. 475 (2023) 214889.
[12] L.-Z. Dong, L. Zhang, J. Liu, Q. Huang, M. Lu, W.-X. Ji, Y.-Q. Lan, Stable heterometallic cluster-based organic framework catalysts for artificial photosynthesis, Angew. Chem. Int. Ed. 59 (2020) 2659–2663.
[13] H. Li, R. Li, G. Liu, M. Zhai, J. Yu, Noble-metal-free single- and dual-atom catalysts for artificial photosynthesis, Adv. Mater. 35 (2023) 2301307.
[14] S. Chen, Y. Qi, C. Li, K. Domen, F. Zhang, Surface strategies for particulate photocatalysts toward artificial photosynthesis, Joule 2 (2018) 2260–2288.
[15] J. Ran, M. Jaroniec, S.-Z. Qiao, Cocatalysts in semiconductor-based photocatalytic CO_2 reduction: achievements, challenges, and opportunities, Adv. Mater. 30 (2018) 1704649.
[16] Y.-Z. Cheng, W. Ji, P.-Y. Hao, X.-H. Qi, X. Wu, X.-M. Dou, X.-Y. Bian, D. Jiang, F.-T. Li, X.-F. Liu, D.-H. Yang, X. Ding, B.-H. Han, A fully conjugated covalent organic framework with oxidative and reductive sites for photocatalytic carbon dioxide reduction with water, Angew. Chem. Int. Ed. 62 (2023) e202308523.
[17] L. Wang, B. Zhu, J. Zhang, J.B. Ghasemi, M. Mousavi, J. Yu, S-scheme heterojunction photocatalysts for CO_2 reduction, Matter 5 (2022) 4187–4211.
[18] J. Xiong, H. Li, J. Zhou, J. Di, Recent progress of indium-based photocatalysts: classification, regulation and diversified applications, Coord. Chem. Rev. 473 (2022) 214819.
[19] Y.-F. Mu, C. Zhang, M.-R. Zhang, W. Zhang, M. Zhang, T.-B. Lu, Direct Z-scheme heterojunction of ligand-free $FAPbBr_3$/α-Fe_2O_3 for boosting photocatalysis of CO_2 reduction coupled with water oxidation, ACS Appl. Mater. Interfaces 13 (2021) 22314–22322.
[20] H. Wang, L. Zhang, Z. Chen, J. Hu, S. Li, Z. Wang, J. Liu, X. Wang, Semiconductor heterojunction photocatalysts: design, construction, and photocatalytic performances, Chem. Soc. Rev. 43 (2014) 5234–5244.
[21] J. Low, J. Yu, M. Jaroniec, S. Wageh, A.A. Al-Ghamdi, Heterojunction photocatalysts, Adv. Mater. 29 (2017) 1601694.
[22] H.S. Moon, K.-C. Hsiao, M.-C. Wu, Y. Yun, Y.-J. Hsu, K. Yong, Spatial separation of cocatalysts on Z-scheme organic/inorganic heterostructure hollow spheres for enhanced photocatalytic H_2 evolution and in-depth analysis of the charge-transfer mechanism, Adv. Mater. 35 (2023) 2200172.
[23] S. Chen, J.J.M. Vequizo, Z. Pan, T. Hisatomi, M. Nakabayashi, L. Lin, Z. Wang, K. Kato, A. Yamakata, N. Shibata, T. Takata, T. Yamada, K. Domen, Surface modifications of $(ZnSe)_{0.5}(CuGa_{2.5}Se_{4.25})_{0.5}$ to promote photocatalytic Z-scheme overall water splitting, J. Am. Chem. Soc. 143 (2021) 10633–10641.
[24] K. Su, S.-X. Yuan, L.-Y. Wu, Z.-L. Liu, M. Zhang, T.-B. Lu, Nanoscale janus Z-scheme heterojunction for boosting artificial photosynthesis, Small 19 (2023) 2301192.
[25] S. Yoshino, A. Iwase, Y. Yamaguchi, T.M. Suzuki, T. Morikawa, A. Kudo, Photocatalytic CO_2 reduction using water as an electron donor under visible light irradiation by Z-scheme and photoelectrochemical systems over $(CuGa)_{0.5}ZnS_2$ in the presence of basic additives, J. Am. Chem. Soc. 144 (2022) 2323–2332.
[26] H. Wang, H. Wang, Z. Wang, L. Tang, G. Zeng, P. Xu, M. Chen, T. Xiong, C. Zhou, X. Li, D. Huang, Y. Zhu, Z. Wang, J. Tang, Covalent organic framework photocatalysts: structures and applications, Chem. Soc. Rev. 49 (2020) 4135–4165.
[27] W. Li, A. Elzatahry, D. Aldhayan, D. Zhao, Core-shell structured titanium dioxide nanomaterials for solar energy utilization, Chem. Soc. Rev. 47 (2018) 8203–8237.
[28] M. Ou, W. Tu, S. Yin, W. Xing, S. Wu, H. Wang, S. Wan, Q. Zhong, R. Xu, Amino-assisted anchoring of $CsPbBr_3$ perovskite quantum dots on porous g-C_3N_4 for enhanced photocatalytic CO_2 reduction, Angew. Chem. Int. Ed. 57 (2018) 13570–13574.
[29] Z. Jiang, X. Xu, Y. Ma, H.S. Cho, D. Ding, C. Wang, J. Wu, P. Oleynikov, M. Jia, J. Cheng, Y. Zhou, O. Terasaki, T. Peng, L. Zan, H. Deng, Filling metal-organic framework mesopores with TiO_2 for CO_2 photoreduction, Nature 586 (2020) 549–554.
[30] N.-Y. Huang, H. He, S.-J. Liu, H.-L. Zhu, Y.-J. Li, J. Xu, J.-R. Huang, X. Wang, P.-Q. Liao, X.-M. Chen, Electrostatic attraction-driven assembly of a metal-organic framework with a photosensitizer boosts photocatalytic CO_2 reduction to CO, J. Am. Chem. Soc. 143 (2021) 17424–17430.
[31] W. Li, J. Liu, D. Zhao, Mesoporous materials for energy conversion and storage devices, Nat. Rev. Mater. 1 (2016) 16023.
[32] H. Huang, R. Shi, Z. Li, J. Zhao, C. Su, T. Zhang, Triphase photocatalytic CO_2 reduction over silver-decorated titanium oxide at a gas-water boundary, Angew. Chem. Int. Ed. 61 (2022) e202200802.
[33] A. Zhou, Y. Dou, C. Zhao, J. Zhou, X.-Q. Wu, J.-R. Li, A leaf-branch TiO_2/carbon@MOF composite for selective CO_2 photoreduction, Appl. Catal. B 264 (2020) 118519.
[34] Y. Wu, Z. Liu, Y. Li, J. Chen, X. Zhu, P. Na, Construction of 2D–2D TiO_2 nanosheet/layered WS_2 heterojunctions with enhanced visible-light-responsive photocatalytic activity, Chin. J. Catal. 40 (2019) 60–69.
[35] K. Lan, R. Wang, W. Zhang, Z. Zhao, A. Elzatahry, X. Zhang, Y. Liu, D. Al-Dhayan, Y. Xia, D. Zhao, Mesoporous TiO_2 microspheres with precisely controlled crystallites and architectures, Chem 4 (2018) 2436–2450.
[36] M.R. Kember, P.D. Knight, P.T.R. Reung, C.K. Williams, Highly active dizinc catalyst for the copolymerization of carbon dioxide and cyclohexene oxide at one atmosphere pressure, Angew. Chem. Int. Ed. 48 (2009) 931–933.
[37] J.-S.M. Lee, A.I. Cooper, Advances in conjugated microporous polymers, Chem. Rev. 120 (2020) 2171–2214.
[38] C. Palladino, T. Fantoni, L. Ferrazzano, B. Muzzi, A. Ricci, A. Tolomelli, W. Cabri, New mechanistic insights into the copper-free heck−cassar−sonogashira cross-coupling reaction, ACS Catal. 13 (2023) 12048–12061.
[39] W. Zhou, H. Shen, Y. Zeng, Y. Yi, Z. Zuo, Y. Li, Y. Li, Controllable synthesis of graphdiyne nanoribbons, Angew. Chem. Int. Ed. 59 (2020) 4908–4913.
[40] J. Li, X. Gao, B. Liu, Q. Feng, X.-B. Li, M.-Y. Huang, Z. Liu, J. Zhang, C.-H. Tung, L.-Z. Wu, Graphdiyne: a metal-free material as hole transfer layer to fabricate quantum dot-sensitized photocathodes for hydrogen production, J. Am. Chem. Soc. 138 (2016) 3954–3957.
[41] G.-Y. Qiao, D. Guan, S. Yuan, H. Rao, X. Chen, J.-A. Wang, J.-S. Qin, J.-J. Xu, J. Yu, Perovskite quantum dots encapsulated in a mesoporous metal-organic framework as synergistic photocathode, Mater. J. Am. Chem. Soc. 143 (2021) 14253–14260.
[42] Y.-N. Gong, L. Jiao, Y. Qian, C.-Y. Pan, L. Zheng, X. Cai, B. Liu, S.-H. Yu, H.-L. Jiang, Regulating the coordination environment of MOF-templated single-atom nickel electrocatalysts for boosting CO_2 reduction, Angew. Chem. Int. Ed. 59 (2020) 2705–2709.
[43] Y.-N. Gong, W. Zhong, Y. Li, Y. Qiu, L. Zheng, J. Jiang, H.-L. Jiang, Regulating photocatalysis by spin-state manipulation of cobalt in covalent organic frameworks, J. Am. Chem. Soc. 142 (2020) 16723–16731.
[44] H. Zhang, J. Wei, J. Dong, G. Liu, L. Shi, P. An, G. Zhao, J. Kong, X. Wang, X. Meng, J. Zhang, J. Ye, Efficient visible-light-driven carbon dioxide reduction by a single-atom implanted metal-organic framework, Angew. Chem. Int. Ed. 55 (2016) 14310–14314.
[45] Y. Wang, Z. Zhang, L. Zhang, Z. Luo, J. Shen, H. Lin, J. Long, J.C.S. Wu, X. Fu, X. Wang, C. Li, Visible-light driven overall conversion of CO_2 and H_2O to CH_4 and O_2 on 3D-SiC@2D-MoS_2 heterostructure, J. Am. Chem. Soc. 140 (2018) 14595–14598.
[46] J. Bian, Z. Zhang, J. Feng, M. Thangamuthu, F. Yang, L. Sun, Z. Li, Y. Qu, D. Tang, Z. Lin, F. Bai, J. Tang, L. Jing, Energy platform for directed charge transfer in the cascade Z-scheme heterojunction: CO_2 photoreduction without a cocatalyst, Angew. Chem. Int. Ed. 60 (2021) 20906–20914.
[47] J.-J. Liu, S.-N. Sun, J. Liu, Y. Kuang, J.-W. Shi, L.-Z. Dong, N. Li, J.-N. Lu, J.-M. Lin, S.-L. Li, Y.-Q. Lan, Achieving high-efficient photoelectrocatalytic degradation of 4-chlorophenol via functional reformation of titanium-oxo clusters, J. Am. Chem. Soc. 145 (2023) 6112–6122.
[48] J. Ding, X. Guan, J. Lv, X. Chen, Y. Zhang, H. Li, D. Zhang, S. Qiu, H.-L. Jiang, Q. Fang, Three-dimensional covalent organic frameworks with ultra-large pores for highly efficient photocatalysis, J. Am. Chem. Soc. 145 (2023) 3248–3254.

[49] S. Gligorovski, R. Strekowski, S. Barbati, D. Vione, Environmental implications of hydroxyl radicals (•OH), Chem. Rev. 115 (2015) 13051–13092.
[50] G. Shi, Y. Xie, L. Du, X. Fu, X. Chen, W. Xie, T.-B. Lu, M. Yuan, M. Wang, Constructing Cu-C bonds in a graphdiyne-regulated Cu single-atom electrocatalyst for CO_2 reduction to CH_4, Angew. Chem. Int. Ed. 61 (2022) e202203569.
[51] Y. Yang, H.-Y. Zhang, Y. Wang, L.-H. Shao, L. Fang, H. Dong, M. Lu, L.-Z. Dong, Y.-Q. Lan, F.-M. Zhang, Integrating enrichment, reduction and oxidation sites in one system for artificial photosynthetic diluted CO_2 reduction. Adv. Mater. 35 (2023) 2304170.
[52] Y.-N. Gong, B.-Z. Shao, J.-H. Mei, W. Yang, D.-C. Zhong, T.-B. Lu, Facile synthesis of C_3N_4-supported metal catalysts for efficient CO_2 photoreduction, Nano Res. 15 (2022) 551–556.
[53] Y. Li, B. Wei, M. Zhu, J. Chen, Q. Jiang, B. Yang, Y. Hou, L. Lei, Z. Li, R. Zhang, Y. Lu, Synergistic effect of atomically dispersed Ni-Zn pair sites for enhanced CO_2 electroreduction, Adv. Mater. 33 (2021) 2102212.
[54] L. Ran, Z. Li, B. Ran, J. Cao, Y. Zhao, T. Shao, Y. Song, M.K.H. Leung, L. Sun, J. Hou, Engineering single-atom active sites on covalent organic frameworks for boosting CO_2 photoreduction, J. Am. Chem. Soc. 144 (2022) 17097–17109.